Published in final edited form as:

ACS Chem Biol. 2022 August 19; 17(8): 2284–2295. doi:10.1021/acschembio.2c00403.

Serum-stable and selective backbone-*N*-methylated cyclic peptides that inhibit prokaryotic glycolytic mutases

R.H.P. van Neer[1], **P.K. Dranchak**[2], **L. Liu**[3], **M. Aitha**[2], **B. Queme**[2], **H. Kimura**[1], **T. Katoh**[1], **K. P. Battaile**[4], **S. Lovell**[3], **J. Inglese**[2,5], **H. Suga**[1]

[1]Department of Chemistry, Graduate School of Sciences, The University of Tokyo, Tokyo, 113-0033, Japan

[2]National Center for Advancing Translational Sciences, National Institutes of Health, Rockville, Maryland, 20850, USA

[3]Protein Structure and X-ray Crystallography Laboratory, Structural Biology Center, University of Kansas, Lawrence, Kansas, 66045, USA

[4]New York Structural Biology Center, NSLS-II, Upton, NY, 11973, USA

[5]National Human Genome Research Institute, National Institutes of Health, Bethesda, Maryland, 20892 USA

Abstract

N-methylated amino acids are privileged residues of naturally occurring peptides critical to bioactivity. However, *de novo* discovery from ribosome display is limited by poor incorporation of *N*-methylated amino acids (*N*-MeAA) into the nascent peptide chain attributed to a poor EF-Tu affinity for the *N*-methyl-aminoacyl-tRNA. By reconfiguring the tRNA's T-stem region to compensate and tune the EF-Tu affinity we conducted RaPID (Random nonstandard Peptides Integrated Discovery) display of a macrocyclic peptide (MCP) library containing six different *N*-MeAAs. We have here devised a "pool-and-split" enrichment strategy using the RaPID display and identified *N*-methylated MCPs against three species of prokaryotic metal ion-dependent phosphoglycerate mutases. The enriched MCPs reached 57% *N*-methylation with up to three

For correspondence: Hiroaki Suga, hsuga@chem.s.u-tokyo.ac.jp; James Inglese, jinglese@nih.gov.

Author Contributions

HS and JI designed research. RHPvN and JI wrote the manuscript with section input from HS and SL. RHPvN conducted RaPID affinity selection studies; PDK and MA performed and analyzed enzymatic and SPR assays, respectively. RHPvN and JI designed and synthesized peptides. SL and BQ performed structural analysis and modeling. SL, LL and KPB respectively carried out crystallography and data collection. MA conducted iPGM protein production and biotinylation. HK and TK provided technical assistance and expertise with setting up the *in vitro* translation system.

Supporting Information

The Supporting Information is available free of charge at http://pubs.acs.org.

Preparation of enzyme expression construct, enzyme·magnetic bead immobilization, RaPID selection readouts, MALDI-ToF mass spectra of synthesized peptides, functional iPGM enzyme assay panel, expanded crystallographic data, purity characterization of synthesized peptides, and expanded methods for the iPGM functional assay panel and thermal shift assay

Accession codes. Coordinates and structure factors have been deposited to the Worldwide Protein Databank (wwPDB) with the accession codes *C. elegans* • Sa-D2 (7TL7) and *S. aureus* • Sa-D3 (7TL8).

Plasmid deposition. The *E. coli* expression plasmids used in this study to produce the iPGMs, pET21a *Ce*-iPGM-bio (ID 162559), pET21a *Bm*-iPGM-bio (ID 162565), pET21a *Ec*-iPGM-bio (ID 162575), pET21a *Mo*-iPGM-bio (ID 179614), pET21a *Lm*-iPGM (180242), pET21a *Mp*-iPGM (180243), pET21a *Wb*-iPGM (180246), pET21a *Hp*-iPGM-bio (ID 179615) and pET21a *Sa*-iPGM-bio (ID 179523) have been deposited into Addgene. Construct designated with "-bio" can enable site-specific C-terminal biotinylation.

consecutively incorporated *N*-MeAAs, rivalling natural products. Potent nanomolar inhibitors ranging in ortholog-selectivity, strongly mediated by *N*-methylation, were identified. Co-crystal structures reveal an architecturally related Ce-2 ipglycermide active site metal ion-coordinating Cys lariat MCP, functionally dependent on two *cis N*-MeAAs with broadened iPGM species selectivity over the original nematode-selective MCPs. Furthermore, isolation of a novel metal ion-independent *S. aureus* iPGM inhibitor utilizing a phosphoglycerate mimetic mechanism illustrates the diversity of possible chemotypes encoded by the *N*-MeAA MCP library.

Graphic Abstract

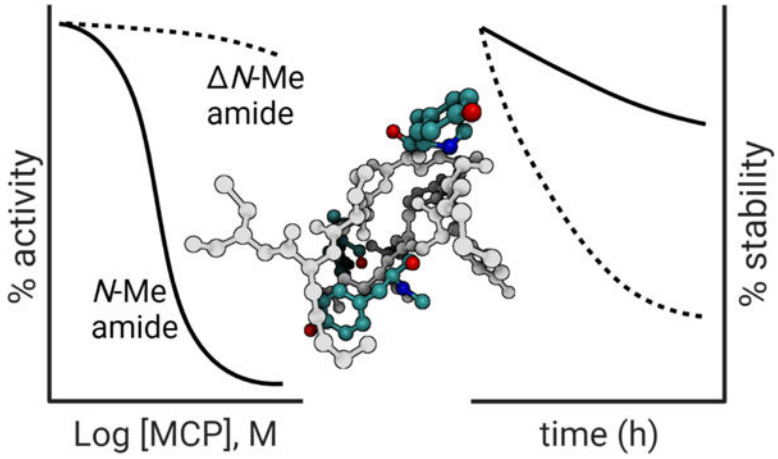

Introduction

N-methylation of peptide backbones can drastically improve a bioactive peptide by improving its weakest characteristics, e.g., metabolic stability and membrane-permeability[1–5]. While many powerful *de novo* discovery tools for peptide ligands have been developed[6], few *de novo* discovered *N*-methylated ligands have been reported. This is caused by the poor ribosomal incorporation of *N*-methylated amino acids (*N*-MeAA) into the nascent peptide chain[7].

Though low in efficiency, *N*-MeAA incorporation is possible, for example, ubiquitin ligase inhibiting macrocyclic peptides have been previously discovered by utilizing a randomized library containing four *N*-MeAA and 11 proteinogenic amino acids (pAA)[8]. These peptides contained *N*-MeAAs upwards to 36% (4/11 residues in the random region), as well as two consecutively incorporated *N*-MeAAs with dissociation constants (K_D) in the sub-nanomolar to nanomolar range. This is significant, as subsequent *N*-methylation of previously discovered peptide ligands often lowers or abolishes the target affinity of the peptide[9–11]. By increasing the number of *N*-MeAAs in the translation system, we would improve the probability and extent of peptide *N*-methylation. However, the poor ribosomal incorporation efficiency of *N*-MeAAs can cause the library to become untranslatable if too many are included.

The cause of suboptimal ribosomal incorporation of *N*-MeAAs is the weakened affinity of *N*-MeAA-tRNA to elongation factor thermal unstable (EF-Tu) compared to natural pAA-

tRNAs due to the steric clashes caused by the *N*-methyl residue with the tight binding pocket in which the pAA amine conventionally resides[12, 13]. The affinity between pAA-tRNA and EF-Tu is mediated by the acylated residue as well as the tRNA T-stem domain. In pAA-tRNAs, the T-stem domain compensates the pAA-mediated EF-Tu affinity, resulting in near equal affinity for all pAA-tRNAs[14]. By preparing a series of tRNAs with increasingly strong binding T-stem domains and pairing them to *N*-MeAAs, a similar affinity balance could be achieved, significantly improving the ribosomal incorporation of *N*-MeAAs and allowing for the *in vitro* translation of a cyclic peptide containing nine different *N*-MeAAs[15]. Here, we applied this methodology to generate a randomized cyclic peptide library containing six *N*-MeAAs and 16 pAAs (Figure 1a). Compared to our previous library[8], this library increases *N*-MeAAs from four to six and total available AAs from 15 to 22.

We used target-based affinity selection system, referred to as the Random non-standard Peptide Integrated Discovery (RaPID) system, to interrogate and enrich members of the *N*-methylated cyclic peptide library through mRNA display[16,17] against three prokaryotic orthologs of the co-factor independent phosphoglycerate mutase (iPGM) enzymes derived from *Staphylococcus aureus* (*S. aureus*), *Helicobacter pylori* (*H. pylori*), and *Mycoplasma orale* (*M. orale*). iPGM catalyzes the interconversion between 2- and 3-phosphoglycerate in a spring-loaded open-closed-open catalytic cycle and is an essential factor in both glycolysis and gluconeogenesis pathways[18, 19].

Humans and other higher mammals use cofactor-dependent phosphoglycerate mutase (dPGM) a homodimer comprised of 23 kDa subunits that requires 2,3-biphosphoglycerate as a cofactor. Whereas iPGM is a monomeric 56 kDa bi-domain enzyme having a divalent metal ion dependence[20]. Therefore, these structural and catalytic differences between the dPGM and iPGM isozymes may permit selective targeting of an iPGM-dependent pathogen's critical glycolytic pathway without affecting host dPGM-dependent glucose metabolism. However, iPGM appears to be poorly druggable, which has been attributed to the structural dynamics of its catalytic mechanism[21].

In a previous RaPID screen on iPGM from *Caenorhabditis elegans* (*C. elegans*) a new class of high-affinity peptide was uncovered that we have termed Ce-2 ipglycermide, an 8-amino acid macrocycle with an extra-cyclic 6-amino acid sequence terminating in Cys14 (Table 1), which is cradled at the interdomain crevice of the open enzyme conformation[22, 23]. The Ce-2 ipglycermide chemotype broadly inhibits iPGMs from parasitic nematodes but exhibits no significant activity on other iPGMs (Table 1). However, many clinically relevant human pathogens utilize iPGM as their glycolytic phosphoglycerate mutase[24–26]. Given the significant sequence similarity among iPGM orthologs and the demonstrated high affinity of ipglycermides across nematode iPGMs, we set out to examine the potential for cross-species selectivity among prokaryotic iPGMs. As such we can expand the infectious disease indications for iPGM inhibitors, and draw on a "one target, many diseases" concept.

To investigate the diversity of ipglycermide chemotypes and expand iPGM selectivity with RaPID technology we employed a pooled target selection strategy, illustrated in Figure 1b, with *S. aureus*, *H. pylori* and *M. orale* iPGMs to identify cross-prokaryotic ortholog and ortholog specific ipglycermides. By incorporating a translation system containing six

N-MeAAs, we aim to discover novel *N*-methyl amide containing iPGM macrocyclic peptide (MCP) inhibitors embodying natural product-like characteristics.

Results and discussion

Library construction

Two cyclic peptide libraries were constructed from a semi-randomized mRNA library following the translation codon table as shown in Figure 1a. In one of the libraries, the initiation AUG codon was reprogrammed to encode for ClAc-L-Tyr, whereas ClAc-D-Tyr was used in the other library. Following AUG, the libraries contain 7 to 15 randomized NNK codons followed by a fixed CGSGSGS linker and an amber stop codon. Ligation of the mRNA to a puromycin linker ensures the encoding mRNA is displayed on the peptide's *C*-terminus. Following *in vitro* translation, the peptide spontaneously undergoes intramolecular cyclization through nucleophilic attack by a cysteine thiolate with the *N*-terminal ClAc group.

Pool-and-split RaPID selection

Unlike the conventional single target RaPID selection scheme, we opted to use a new multi-target "pool-and-split" selection approach where several orthologous targets are initially mixed to discover both ortholog-selective and non-selective prokaryotic iPGM inhibitors (Figure 1b). The bead immobilization efficiency of the three iPGM orthologs was individually determined to be 10 pm/μL bead slurry for *S. aureus* iPGM, 20 pm/μL for *H. pylori* iPGM and 30 pm/μL for *M. orale* iPGM (Supplementary Figure 1). Using these immobilization densities, the immobilized iPGMs were mixed as a 1:1:1 ratio. During the first three cycles of RaPID, the peptide libraries were selected with this iPGM mixture. On the fourth round, the pre-enriched libraries were split into three and individually screened against either *S. aureus*, *H. pylori*, or *M. orale* iPGM until enrichment of the library was observed (Supplementary Figure 2). The individual MCPs are designated by the final iPGM selection enzyme and initiator amino acid stereochemistry, D or L defining the library (see ID column in Table 1).

The efficacy of the new T-stem tuned translation system is demonstrated by the sequences of the enriched peptides. Poor incorporation of *N*-MeAAs would have caused highly methylated peptides to be eliminated in favor of more efficiently translated candidates bearing less methylation. Nevertheless, the peptides identified in the final selection were highly methylated with upwards of three consecutive *N*-MeAAs and 57.1% total methylation (8/14) in the random region (Table 1, peptide Hp-L2). Most peptides contain more *N*-MeAAs than the average 27.3% (6/22) of available residues, suggesting that the *N*-MeAAs are both well incorporated and generally beneficial to the binding affinity.

Functional characterization of ligands

The 10 MCPs were synthesized by solid phase peptide synthesis (SPPS; Supplementary Figure 3) and functionally characterized with a luminescent coupled-enzyme ATP-quantifying assay against a panel of iPGM orthologs[23]. The panel contained representative iPGM species orthologs derived from the nematodes, *C. elegans*, *Brugia malayi* (*B. malayi*)

and *Wuchereria bancrofti* (*W. bancrofti*), prokaryotic forms from *Escherichia coli* (*E. coli*.), *Mycoplasma pneumoniae* (*M. pneumoniae*), *S. aureus*, *H. pylori*, *M. orale*, and the phylogenetically more distant trypanosome, *Leishmania mexicana* (*L. mexicana*). Overall, the MCPs display a broad range of inhibitory potencies and selectivity. The MCP sequence and apparent IC_{50} values derived from concentration-response curves (CRCs) on each iPGM ortholog are shown in Table 1 and Supplemental Figure 4a, respectively.

Several observations were made from the functional activity profiling, the most salient of which were potent nanomolar activity (see bold entries in Table 1) of *M. orale* and *S. aureus*-selected MCPs (e.g., Mo-L2, -D1, -D2 and Sa-D2, -D3) on *M. orale* iPGM, whereas on *S. aureus* iPGM these MCPs were inactive or >10-fold less potent. Notwithstanding, Sa-D3 is remarkably potent (45 nM) on *S. aureus* iPGM. The potency and selectivity distribution of MCPs varied depending on the iPGM ortholog used in the final selection (Figure 1b). For *H. pylori* iPGM, MCPs Hp-L2 and -D3 were obtained ranging between 7 μM−16 nM across prokaryotic and nematode iPGMs, showing moderate potency on *H. pylori* iPGM (1–6 μM). For the four *M. orale* iPGM selected MCPs studied, all but one (Mo-L1) displayed high *M. orale* iPGM selectivity and very high inhibitory potency, with Mo-L2, -D1 and -D2 having IC_{50} values between ~2 and 11 nM. MCPs undergoing the final enrichment step with *S. aureus* iPGM resulted in an intermediate distribution of iPGM selectivity. While the most potent *S. aureus* iPGM MCPs observed in this study were obtained from the *S. aureus* iPGM enrichment (Sa-D3), this enrichment step yielded the highest potency panortholog iPGM MCP, As well as the only Ce-2 ipglycermide lariat-like MCP, Sa-D2, having an IC_{50} range between 2–400 nM across 7 of the 9 iPGMs profiled was isolated in this selection.

Essential nature of methylation on binding activity and serum stability

To investigate the effect amide *N*-methylation has on the binding of the discovered peptides, amide (ΔMe) analogs of eight MCPs were prepared and characterized with the same activity-based enzyme assays, the results of which are summarized in Table 1. In most of the assayed peptides, loss of *N*-methylation leads to a near complete loss of inhibitory activity (Figure 2a–c) and reduction in serum stability (Figure 2d–f).

As illustrated in Figure 2e, *N*-methylation can significantly improve a peptide's serum stability but does not do so universally. In fact, in one example, peptide Mo-L1, we found that *N*-methylation lowered the peptide's serum stability (Figure 2f). Here, the structural shift induced by the *N*-methyl groups may result in a peptide topology where the endopeptidase cleavage site is more exposed than it would be in an all-pAA peptide. Nevertheless, in half of the peptide pairs analyzed we found considerable improvement of serum stability mediated by the presence of *N*-methylation. Remarkably, it appeared that the peptides Mo-L2 and Mo-D2 are completely resistant to degradation by serum-borne metabolic enzymes.

This data suggest *N*-methylation appears to affect the MCP conformation so significantly that retention of the combinatorial effect on activity and metabolic stability after conversion between proteogenic amide and *N*-methyl amide backbone residues is exceptionally unlikely. These results, therefore, demonstrate the potential advantage of incorporating *N*-MeAAs during the discovery phase of peptide ligands, rather than during the medicinal

chemistry phase of lead optimization to have maximal impact of *N*-methylation on MCP activity and metabolic stability.

Sa-D2, a lariat macrocyclic structure, shares a Ce-2 inhibitory mechanism

Of the analyzed MCPs, Sa-D2 stands out displaying potent, cross-ortholog affinity and inhibitory activity, structurally resembling the terminal Cys lariat structure of Ce-2 Ipglycermide but having a larger macrocycle and a shorter extra cyclic extension (Figure 3a and Table 1). Based on this, Sa-D2 may utilize the same inhibition mode as Ce-2; a thiolate-metal ion coordinated interaction. Unlike Ce-2, however, Sa-D2 appears to either interact with a more conserved iPGM binding site, and/or requires fewer contacts allowing the MCP to strongly inhibit both nematode and prokaryotic iPGM orthologs rather than displaying the potent nematode iPGM selectivity of Ce-2 Ipglycermide.

The Sa-D2 − *C. elegans* iPGM binding kinetics derived K_D = 1.8 nM and $t_{½=}$ 15 min (Figure 3b), are within the same order of magnitude observed for Ce-2 binding to the *C. elegans* iPGM, *B. malayi* ortholog (K_D = 0.5 nM, $t_{½}$= 52 min), despite *C. elegans* iPGM sharing 71% and 40% identity with *B. malayi* and *S. aureus* iPGM, respectively[22, 23]. This suggests that cross-species ortholog inhibitors, such as Sa-D2 are more likely to be derived from pool-and-split selection approaches. Interestingly, though demonstrating inhibitory activity on *M. orale* and *H. pylori* iPGM, Sa-D2 does not inhibit *S. aureus* iPGM despite appearing to bind strongly based on SPR analysis (Figure 3a, c).

The observation that Sa-D2 can bind to *S. aureus* iPGM but not inhibit the functional enzyme activity explains how Sa-D2 was enriched by *S. aureus* iPGM in the final affinity selection rounds. The lack of functional activity is likely because enzymatically active *S. aureus* iPGM requires Mn^{2+}, whereas the thiolate-coordinating complex is only achievable with a Zn^{2+} containing enzyme. Supporting this is the absence of a significant thermal shift in the melting temperature of active *S. aureus* iPGM by Sa-D2 (Figure 3d; ΔT_m=3°C). Whereas, the non-thiolate containing inhibitor Sa-D3, which functionally inhibits (Table 1) and displays measurable binding kinetics (K_D = 790 nM, $t_{½}$= 27 s; Figure 3e) clearly stabilized the melting temperature (ΔT_m= 17°C) of the enzyme. Taken together, this suggests that Sa-D2 strongly binds to the minority of inactive Zn^{2+} coordinating *S. aureus* iPGM but lacks affinity to the active Mn^{2+} coordinating enzyme.

To further investigate binding requirements of the Sa-D2 structure, four additional Sa-D2 analogs were prepared and characterized on the iPGM enzyme panel. These MCPs include a Cys13Ser substitution (Sa-D2 C13S), a truncation of the extra cyclic sequence, Pro11Lys12Cys13 (Sa-D2 ΔPKC), and the larger 13 amino acid macrocyclic analog (Sa-D2 LgMC). The effects of each modification on inhibitory activity, shown in Table 1 and Supplementary Figure 4b, were either lost or significantly diminished. These observations reinforce the hypothesis that, like Ce-2 Ipglycermide, the second cysteine (Cys13) of Sa-D2 is also anchored into the iPGM metal-binding site and may have a similar, though more ortholog-ambiguous mode of action. However, despite either relocation of the free thiol to the interior of the MCP (*i.e.*, Sa-D2 LgMC) or substitution for a non-nucleophilic residue (Sa-D2 C13S), both analogs retained some ability to either inhibit or only bind an iPGM (Table 1 and Supplementary Figure 4a). In contrast, the apparently minor modification of

substituting the *N*-methyl amides at Tyr5 and Tyr8 for amides in either Sa-D2 (Sa-D2 Δ*N*-Me) or Sa-D2 LgMC (Sa-D2 LgMC Δ*N*-Me) results in total loss of the cyclic peptide activity (Supplementary Figure 4b), suggesting a key structural role required for Sa-D2 activity.

Sa-D2 • *C. elegans* iPGM co-crystal structure: limited contacts contribute to broad iPGM species selectivity

For a Sa-D2 • *C. elegans* iPGM complex we obtained crystals diffracting to 1.90 Å having clearly defined electron density maps permitting all atoms for the cyclic peptide to be modeled except for the sidechain of Arg2 (Supplementary Figure 5a). At the phosphotransferase domain, Sa-D2 forms hydrogen bond interaction with G145, R216 and D286 as depicted in Figure 4a.* Tyr6 of Sa-D2 binds in the same basic region near R284 (Figure 4b), in proximity to the 3PG binding site, as the position 7 aromatic amino acid substitutions, Phe, His and Tyr, observed in the co-crystal structures of Ce-2 Y7F (PDB: 7KGN), Ce-2 Y7H C14NHOH (PDB: 7KNF) and Ce-2d (PDB: 5KGN), respectively[22, 23]. Further, the sidechain carboxylate of Sa-D2 Glu9 approaches R284 from the opposite side as Tyr6 as shown in Figure 4b. Superposition of the *C. elegans* iPGM co-crystal structures bound to Ce-2 Y7F and Sa-D2 yielded an RMSD deviation of 2.30 Å between Cα atoms (291 residues). Although the overall domain structures are similar, the secondary structure elements are offset slightly, particularly in the transferase domain, though the proximity of Tyr6 in Sa-D2 to Phe7 in Ce-2 Y7F can clearly be observed (Figure 4c).

The terminal Cys13 residue sidechain interacts with the Zn^{2+} ion through the S-atom (2.32 Å). This Zn^{2+} ion coordination resembles that observed for *C. elegans* iPGM in complex with the Ce-2 ipglycermide analog, Ce-2 Y7F (PDB 7KNG) however, the orientation of the Sa-D2 is strikingly different. Notably, although the two peptides ultimately coordinate a Zn^{2+} ion via their C-terminal Cys residues, the orientations in the binding pocket are markedly different (Figure 4c and Supplementary Figure 5b). This may be due to the larger cyclic portion of Sa-D2 versus Ce-2 Y7F which have 10 and 8-membered macrocycles respectively.

Strikingly, we observe both the Tyr5 and Tyr8 *N*-methyl amides of Sa-D2 adopt the *cis* configuration as shown in Figure 4d. The amide carbonyl of Tyr8 is positioned to hydrogen bond with N85, a phosphatase domain residue conserved among the iPGMs, proximal to the Cys13 thiolate–Zn^{2+} coordinating interaction (Figure 4a). In the Ce-2 Y7F structure, the neighboring E87 engages with Thr13 potentially reinforcing the Cys14 thiolate–Zn^{2+} interaction. Interestingly, these conserved iPGM residues, N85 and E87 are located on either side of S86, the serine nucleophile at the center of the catalytic mechanism of phosphoglycerate isomerization.

Overall Sa-D2, not surprisingly, shares only key binding interactions with highly conserved residues and regions shared by prokaryotic and nematode iPGMs. Unlike the extensive interactions Ce-2 ipglycermides make with the Hinge 1 and 2 regions of nematode iPGMs,

*In the text, the single-letter amino acid convention is used to denote protein residues and sequences, whereas the three-letter code is used in descriptions of the peptide macrocycles, and when preceded by “Me” indicates the *N*-methyl amide.

there are no residues from Sa-D2 that venture into this area of relatively low conservation between nematode and prokaryotic iPGMs (Figure 4c).

The Sa-D3 macrocycle features a 3PG mimetic carboxylate

Sa-D3 represents the majority of ipglycermides structures identified in this study, having exclusively a macrocyclic configuration without a free thiolate-bearing linear tail region. To explore the novel inhibitory mechanism of Sa-D3 we obtained the co-crystal structure of this ligand with *S. aureus* iPGM (Figure 5a). The electron density maps for Sa-D3 were clearly defined and all atoms for the macrocycle could be modeled (Supplementary Figure 5c). Along with the native diffraction data, a second data set was collected from another crystal at a wavelength of 1.3Å, which is on the low-energy side of the Zn^{2+} absorption edge. A strong anomalous signal was observed at the metal-binding sites (Supplementary Figure 5d) suggesting occupancy by Mn^{2+} ions, in agreement with previous literature[19, 20]. The Mn^{2+} ions interact with D397, H401, H456 and three water molecules at site 1 and D12, S62 (the active-site serine nucleophile equivalent to S86 in *C. elegans* iPGM), D438 and H439 at site 2 (Supplementary Figure 5d).

The cyclic peptide forms hydrogen bond interactions with the backbone carbonyl of Trp6 and Q77 Nε; the backbone carbonyl of Trp7 and D78 Oγ; the backbone carbonyl of *N*-Me Ser9 Oγ and R257 NH1; the backbone carbonyl of Glu12 and R257 NH1; the backbone carbonyl of Asp13 and R257 NH1; the backbone carbonyl of Asp13 and R191 NH1; the side chain of Asp13 OD2 and R191 NH1 and the side chain of Asp13 OD2 and R260 Nε (Figure 5a–b). The latter hydrogen bonds between Asp13 of the cyclic peptide and R191/R260 of *S. aureus* iPGM form strong interactions between residues of opposite charge.

We had observed that the single *N*-Me amide (Ser9) had a marginal contribution to the inhibitory potency and binding kinetics of Sa-D3 on *M. orale* and *S. aureus* iPGMs (Table 1 and Figure 3f). Notably, unlike the *cis* configurations observed for the *N*-methyl amides of Sa-D2, the Ser9 *N*-methyl amide adopts the lower energy *trans* configuration (Figure 5a).

Sa-D3 has a surface area of 1594.2 $Å^2$ and 924.1 $Å^2$ of this total area is buried within the *S. aureus* iPGM interdomain cleft. Residues D-Tyr1, Trp6 and Trp7 are snuggly fit within pockets of the binding site (Figure 5c). Similarly, Trp11 is positioned within a relatively neutral cleft and Asp13 occupies a positively charged pocket-forming the interactions noted above (Figure 5d). Interestingly, the side chain of Glu12 does not form interactions with the Arg residues in this region and is directed away from the iPGM surface presumably due to the proximity of D154 which repels the side chain.

The overall *S. aureus* iPGM complex with the Sa-D3 peptide is quite similar to previously determined *S. aureus* iPGM structures. Notably, the superposition of *S. aureus* iPGM•Sa-D3 with apo *S. aureus* iPGM (PDB 4MY4[19]) and 3-phosphoglycerate bound *S. aureus* iPGM (PDB 4NWJ[19]) yielded RMSD deviations between Cα atoms of 0.99 Å (484 residues) and 0.97 Å (485 residues) respectively. The 3-phosphoglycerate molecule in 4NWJ occupies a position between Glu12 and Asp13 of the Sa-D3 peptide as observed in the superposition of co-crystal structures 7TL8 and 4NWJ shown in Figure 5e.

Conclusion

Tuning the affinity of *N*-MeAA-tRNA to EF-Tu via the T-stem domain (Figure 1a) enables the ribosomal synthesis of more exotic *N*-MeAA containing peptides than previously possible, allowing for screening and discovery of heavily *N*-methylated MCPs. Using this method we discovered a broad variety of *N*-methylated MCPs targeting prokaryotic iPGMs containing between one and eight *N*-MeAAs (Table 1). Interestingly, as determined with respective non-*N*-methylated MCP analogs, the *N*-methylation state of the peptide may have a range of effects on the MCP to act as an inhibitor of a given iPGM which generally aligns with its binding kinetics (Table 1 and Figure 2). In our limited evaluation of *N*-methylation state on metabolic stability we observed that in some cases *N*-methylation greatly prevented the serum protease degradation of the MCP, as seen with Mo-D1 and Mo-D2, or had minimal to no discernable effect in others, while in one case, Mo-L1 *N*-methylation hastened its degradation (Figure 2f).

In our previous studies we obtained nematode iPGM selective ipglycermide Ce-2 (Table 1) using *C. elegans* iPGM for the affinity selection[23]. To increase the probability of isolating cross-iPGM ortholog selective MCPs we pooled three prokaryotic iPGMs to initially enrich the library, performing the final selections on the individual enzymes (Figure 1b). The approach successfully isolated several potent cross species inhibitors, as well as highly selective MCPs where potency is tightly tied to *N*-methylation state (e.g., see Mo-L/D series Table 1). Remarkably, while *S. aureus* iPGM captured Sa-D2, a potent nematode and *M. orale* iPGM inhibitor, this MCP has no significant inhibitory activity on *S. aureus* iPGM (Figure 3a and Table 1). We speculate that a fraction of *S. aureus* iPGM contains Zn^{2+} and represents the functionally inactive species that bound Sa-D2 resulting in the observable signal by SPR (Figure 3c). Whereas, under thermal shift conditions (e.g., $[E]>>K_D$), Sa-D3 stabilized the enzyme from thermal denaturation while Sa-D2 fails to do so (Figure 3d), further suggesting any Zn^{2+} species is a minor component.

Co-crystal structures of two iPGM•MCP complexes provide insight into the structural basis for novel binding modes, cross-ortholog selectivity, and define the stereochemistry around the *N*-methyl amide residues in Sa-D2 and Sa-D3. Unexpectedly, we observed that the two *N*-methyl amides required for Sa-D2 activity reside in the *cis* configuration (Figure 4d), while in Sa-D3 we observe a *trans* configuration for the single, non-essential *N*-methyl amide (Figure 5e). Sa-D2, having a cys-terminal lariat coordinates the active-site Zn^{2+} correspondingly to the previously reported Ce-2 ipglycermide, but with expanded cross-ortholog activity, likely resulting from the remainder of the macrocycle making fewer interactions and concentrated at non-conserved regions of the enzyme (Figure 4c). Sa-D3 represents a completely novel non-lariat macrocycle inhibitor that acts as a 3-phosphoglycerate mimetic stabilized by a hydrophobic interaction mediated by Tyr1 (Figure 5c). In this structure Asp13 forms ionic bonds with the basic phosphoglycerate-binding region formed by R191, R257 and R260 (Figure 5d). Interestingly, Glu12 may present a repulsive interaction with D154.

In summary, we demonstrated the *de novo* incorporation of *N*-methylation into high affinity MCPs and the impact these privileged residues have on target affinity and metabolic

stability. Above all, the number of potent and structurally varied MCPs we discovered that target iPGMs with cross-ortholog selectively demonstrates that the isolated success of Ce-2 was not just a lucky coincidence. In fact, these results demonstrate that iPGM can no longer be considered as an undruggable target and pave the way for the potential development of an entirely new class of antimicrobials.

Materials and methods

In vitro translation system.

The Flexizymes dFx and eFx, as well as mRNAs were prepared as previously reported [27]. T-stem appropriate tRNAs were matched to their respective residues and prepared as previously reported [15]. Cyanomethyl ester (CME) and 3,5-dinitrobenzyl ester (DBE) activated amino acids $_{Me}Y^{(OMe)}$-CME, $_{Me}$F-CME, $_{Me}$S-DBE, $_{Me}$Nle-DBE, $_{Me}$Y-CME, $_{Me}$G-DBE, and ClAc-(L/D)-Y-CME were prepared as previously reported [7, 27, 28]. The cell free translation system used in this study was previously optimized [29, 30], and adapted for the translation of N-methylated peptides [15].

Macrocyclic library design—The macrocyclic peptide library was constructed as a standard RaPID selection library with 7–5 randomized residues encoded by NNK codons and initiated with either ClAc-L-Tyr or ClAc-D-Tyr [31]. The prepared DNA library was transcribed, ligated to puromycin, *in vitro* translated, and reverse transcribed prior to affinity selection against iPGMs.

Affinity selection and enrichment—Prior to the selections, immobilization rates of the three iPGM targets, *S. aureus* iPGM-His6, *H. pylori* iPGM-His10, and *M. orale* PGM-His10, to Dynabeads His-tag Isolation & Pulldown (Invitrogen) were determined to be 10 pm/μL for, 20 pm/μL, and 30 pm/μL respectively (Supplementary Figure 1).

The N-methylated mRNA-puromycin conjugated MCP libraries described above were synthesized by *in vitro* translation, reverse transcribed and subsequently desalted with Sephadex G-25 (Cytiva) in PBST. From this desalted solution, 0.5 μL was diluted 1000x as an input quantification sample. The libraries were cleared 6x with Dynabeads His-tag Isolation & Pulldown to remove His-tag binding peptides and His-tagged proteins of the FIT system from the solution. The three iPGM orthologs were immobilized onto Dynabeads at the previously established saturation points and mixed to have equal quantities of each orthologue in the final mix. The MCP library was incubated with 67 nM of each immobilized iPGM with 200 nM total iPGM for 30 min. The beads were washed, and cDNA of binding peptide was quantified by qPCR and amplified by PCR. The amplified cDNA was transcribed into mRNA and the method repeated using this new library. In round 2, following the desalting step of the MCP library, blocking buffer containing acetylated BSA and yeast RNA was added to limit nonspecific binding. Furthermore, cDNA of MCPs binding to the last set of negative beads was eluted and quantified by qPCR to monitor enrichment of bead binding MCPs.

During round 4, the MCP libraries were split into 3 and overlaid onto 200 nM each of the three individual, immobilized iPGM orthologs separately. The six MCP libraries that

resulted from this were further enriched until an exponential increase in recovery was observed by qPCR. This happened at round five for all libraries except the ClAc-D-Tyr initiated library enriching against *S. aureus* iPGM, which required an additional round. After enrichment was observed (Supplementary Figure 2), the cDNA of the libraries was analyzed by next-generation sequencing and enriched peptides were identified.

Chemical synthesis of N-methylated MCPs—Precyclized peptides were synthesized by standard Fmoc automated SPPS at a 25 μmol scale using Rink Amide resin [32]. Standard couplings were conducted using HOBt/HBTU at 30°C for 40 minutes twice. Couplings to N-methylated amines were conducted using HOAt/HATU at 60°C for 40 minutes twice. Tyr(Me) was manually N-methylated via on-resin Mitsunobu coupling [33]. Peptides that contained multiple cysteine residues were prepared using Fmoc-Cys(Mmt)-OH for the cyclizing cysteine and Fmoc-Cys(Dpm)-OH for the others. Following SPPS, the N-termini were chloroacetylated using a 0.2 M solution of chloroacetoxy succinimide ClAc-NHS in DMF. The Mmt group of peptides containing multiple cysteine residues was deprotected with 5% TFA and 2.5% triisopropylsilane in DCM. These peptides were subsequently cyclized on resin by overnight agitation in 5% diisopropyl ethylamine in DMF.

Peptides were deprotected and cleaved off the resin with a 2.5% triisopropylsilane, 2.5% DoDT, 2.5% water in TFA cocktail for 3 h at RT. The resin was filtered, washed with TFA, and concentrated in vacuo followed by precipitation with ice-cold diethyl ether. The precipitated peptides were washed with diethyl ether and dried overnight. The dried peptides were dissolved in DMSO and cyclized by addition of triethylamine if they were not previously cyclized on resin. Peptides were finally purified by reverse-phase preparatory HPLC and identified by MALDI-TOF-MS and analytical UPLC (Supplementary Figure 3, Supplementary Table 3).

Serum stability assay—Human serum stability of the synthesized peptides was assayed similarly as previously described [34]. Both the *N*-methylated peptide and corresponding Δ*N*-Me analogue were mixed with internal control peptide in human serum to a final concentration of 10 μM. Peptides Ce-2 and Ce-2d were paired in a similar manner. At every time point (t= 0, 1, 3, 9, 24, 72h.) 13.5 μL of human serum was mixed with 1.5 μL 100mM TCEP to reduce the sample. Serum proteins were precipitated by addition of 35 μL methanol and incubation on ice for 5 min. The samples were centrifuged, and the supernatant was stored at −20°C until analysis. Immediately prior to analysis the samples were diluted with 9 volumes 1% TFA in water and centrifuged for 5 minutes prior to analysis by UPLC-ESI-MS. To control for serum activity, a canonical, linear peptide was assayed in parallel and observed to be fully degraded in approximately nine hours.

Preparation of iPGM enzyme constructs—*W. bancrofti* iPGM (10xHis C-terminal tag) EJW84318.1; *M. orale* iPGM (10xHis C-terminal tag, 1293A>T to avoid introduction of a premature stop codon during bacterial expression) NZ_LR214940.1; *M. pneumoniae* iPGM (10xHis C-terminal tag), CP010547.1; *H. pylori* iPGM, (10xHis *C*-terminal tag) CP001173.1; *L. mexicana* iPGM (10xHis C-terminal tag), AJ544274; and *S aureus* iPGM (6xHis C-terminal tag), BX571856.1 were cloned into pET21a(+) and transformed into BL21(DE3) for *E. coli* expression as described[23]. For site-specific incorporation of biotin,

the *S. aureus* iPGM was constructed to have the GLNDIFEAQKIEWHE sequence[35] located between the *C*-terminus and His tag as described in Supplementary Methods.

iPGM expression and purification—Expression and purification of the iPGMs (*C. elegans, B. malayi, W. bancrofti, E. coli, S. aureus, M. orale, M. pneumonia, H. pylori* and *L. Mexicana*) were carried out by following the previously described methods.[22, 23] For the functional enzyme assays, 1 mL each of *C. elegans*, *B. malayi, M. orale,* and *S. aureus* iPGMs were supplemented with 10 μL of 10 mM ZnCl2 and 10 μl of 10 mM $MnCl_2$ then dialyzed for 16 hours against 1 L of 1X PGM buffer containing 20% glycerol using Slide-A-Lyzer™ Dialysis Cassettes (Thermo Scientific, Cat# 66380). The dialyzed samples are stored at 4°C up to 8 weeks.

***In vitro* biotinylation—**iPGM (*C. elegans* and *S. aureus*) biotinylation reactions were carried out at 100 μM scale in PBS buffer according to the procedure described in Fairhead and Howarth[35] as applied in Wiedmann et al.[22] Free biotin and *E. coli* Bir-A were removed by loading the reaction mixture onto a HiLoad Sephadex 16/60 prepacked column and eluted at 0.5 mL/min with PGM storage buffer. Biotinylation efficiency was measured using the streptavidin conjugation assay.[35]

PGM enzymatic assays and AC_{50} determinations—Inhibition of phosphoglycerate mutase activity in the presence of macrocyclic peptides was measured as a luminescence end point output assay as previously described[23]. Briefly, 4 μL enzymes were dispensed into white solid-bottom medium bind 1536-well plates (Greiner Bio-One) in a pH 8.0 assay buffer (30 mM Tris-HCl, 5 mM Mg2SO4 and 20 mM KCl) with the BioRaptor FRD (Beckman Coulter). Enzymes were run at the lowest concentration determined to give significant signal when run at an estimated Km substrate concentration (5 nM *Caenorhabditis elegans* and *Brugia malayi* iPGM, 40 nM *Wuchereria bancrofti* iPGM, 8 nM *Mycoplasma orale* and *Mycoplasma pneumoniae* iPGM, 50 nM *Escherichia coli* and *Trypanosoma brucei* iPGM, 10 nM *Staphylococcus aureus* iPGM, and 100 nM *Helicobacter pylori* iPGM), while *H. pylori* iPGM was run in the presence of 5 μM ZnCl2 and *S. aureus* and *T. brucei* iPGMs were run in the presence of 100 μM MnCl2. Assay buffer with no enzyme was added to column 1 of each respective plate as a control. Macrocyclic peptides were prepared at 5 – 20 mM in DMSO and added to enzymes at 23 nL per well transferred by a Pin tool (Wako Inc.) in a 16-pt, 1:3 titration in duplicate spanning a concentration range of 1.3 pM to 76.8 μM along with DMSO and a titration of Ce-2 and Ce-2d positive controls from top concentration 3.8 μM to 0.27 pM in columns 2–4 of each plate. Enzymes were incubated with peptide for >20 min at ambient temperature, protected from light. 2 μL of 3-phosphoglycerate in a coupled enzyme assay buffer (includes enolase and pyruvate kinase) was added to enzyme/peptide mixtures with BioRaptor FRD and reactions were incubated for 5 min at ambient temperature, protected from light for all enzymes except Hp iPGM that was incubated with substrate for 10 min at ambient temperature and *E. coli* iPGM where reactions were incubated at 37°C for 15 min, followed by addition of 4 μL Kinase-Glo Plus reagent (Promega Corporation). Plates were incubated at ambient temperature for 10 min then measured by a ViewLux plate reader (PerkinElmer). See also Supplementary Protocol

Table 1. CRCs were fit and AC_{50} values calculated using nonlinear regression log(inhibitor) vs. response -- Variable slope (four parameters) in Prism (GraphPad Software).

Thermal Shift Assays—Ligand-stabilized iPGM melting temperatures were determined using the Thermofluor method.[36] Briefly, samples were tested in MicroAmp optical 384-well reaction plates (Applied Biosystems by Life Technologies) using a ViiA 7 real time PCR instrument (Applied Biosystems) and the fluorescent dye SYPRO Orange (Life Technologies). The final concentration of protein and dye were maintained at 5 μM and 10x respectively. The proteins were diluted in PBS (10 mM Na2HPO4, 1.8 mM KH2PO4, 137 mM NaCl and 2.7 mM KCl) and added to the 384 well plate, followed by compounds also diluted in PBS (final concentrations between 0 to 100 μM). Samples were incubated for 10 mins at ambient temperature and protected from light. Next, 4 μl of dye solution (initial concentration of 5000x diluted in PBS to 50x) was added to the each well using a multi-channel pipette. The plate was sealed with a MicroAmp optical adhesive film (Applied Biosystems), centrifuged for 1 min at 1000 RPM then loaded on to the real time PCR instrument for data collection after samples were initially cooled to 4 °C for 1 minute then ramping temperature from 4 to 95 °C at 1°/min. increments. The first derivative of the melting data was plotted in GraphPad Prism to determine Tm. A step-by-step detailed assay protocol is described in Supplementary Protocol Table 2.

SPR experiments—SPR experiments were performed using a Biacore S200 instrument at a flow rate between 20–40 μL/min, 25°C using 1X PBP-P as a running buffer as previously described.[22] Briefly, biotinylated iPGMs were immobilized on a Biotin CAPture (CAP) chip. High performance kinetic experiments were performed by injecting a series of macrocyclic peptide concentrations (within 10-fold of K_D). Kinetic and affinity data was analyzed using Biacore S200 Evaluation Software. All sensorgrams were fitted, after background correction to a 1:1 binding model using the BIAevaluation software as previously described.[22].

Crystallization and Data Collection—Purified apo *C. elegans* and *S. aureus* iPGM spanning residues M19−I539 and M26−H538, respectively, both harboring a *C*-terminal hexahistidine tag were concentrated to 12.0 mg/mL (0.2 mM) in 150 mM NaCl, 30 mM Tris pH 8.0, 1 mM TCEP. To prepare the respective Sa-D2 and Sa-D3 cyclic peptide complexes a 20 mM stock solution was prepared in DMSO, mixed in a 1:1.25 (protein:cyclic peptide) molar ratio and incubated on ice for 30 minutes prior to screening. All crystallization experiments were setup using an NT8 drop-setting robot (Formulatrix Inc.) and UVXPO MRC (Molecular Dimensions) sitting-drop vapor diffusion plates at 18 ºC. 100 nL of protein-ligand mixture and 100 nL crystallization solution were dispensed and equilibrated against 50 μL of the latter.

For the *C. elegans*•Sa-D2 complex, crystals displaying a prismatic morphology were observed within approximately 7 days, from the Morpheus Screen HT[37] (Molecular Dimensions) condition H4, which contains the following mixtures: 37.5% (w/v) of precipitant mix 4: (25% (v/v) MPD; 25% (w/v) PEG 1000; 25% (w/v) PEG 3350), 100 mM of MB1 pH 6.5: (1.0 M imidazole, MES), 100 mM of MAA: (0.2 M DL-Glutamic acid monohydrate; 0.2M DL-Alanine; 0.2M Glycine; 0.2M DL-Lysine monohydrochloride; 0.2M

DL-Serine). For the *S. aureus*•Sa-D3 complex, crystals displaying a plate morphology were observed within approximately 14 days from the Index HT Screen (Hampton Research) condition G7, containing 25% (w/v) PEG 3350, 100 mM Bis-Tris pH 6.5, 200 mM ammonium acetate. A cryoprotectant composed of 80% crystallant and 20% PEG 200 was layered onto the drop, samples were harvested and stored in liquid nitrogen for X-ray diffraction data collection.

Structure Solution and Refinement—X-ray diffraction data were collected at the Advanced Photon Source beamline 17-ID using a Dectris Eiger2 9M X detector for *C. elegans*•Sa-D2, and at the National Synchrotron Light Source II (NSLS-II) beamline 19-ID (NYX) using a Dectris Pilatus 6M pixel array detector for *S. aureus*•Sa-D3. Intensities were integrated using XDS[38, 39] via Autoproc[40] and the Laue class analysis and data scaling were performed with Aimless[41] which indicated that the highest probability Laue class was 2/*m*.

Structure solution was conducted by molecular replacement with Phaser[42] using a previously determined isomorphous structure (PDB 7KNF[22]) for *C. elegans*•Sa-D2, and the structure PDB 4MY4[19] for *S. aureus*•Sa-D3, as the respective search models. For *C. elegans*•Sa-D2 the top solution was obtained in the space group $P2_1$ with 4 molecules in the asymmetric unit. For *S. aureus*•Sa-D3 the top solution was obtained in the space group $P2_1$ with a single molecule in the asymmetric unit, and the model was improved by automated model building Buccaneer[43].

For both, structure refinement and manual model building were conducted with Phenix[44] and Coot[45] respectively. Disordered side chains were truncated to the point for which electron density could be observed. Structure validation was conducted with Molprobity[46] and figures were prepared using the CCP4MG package[47]. Superposition of iPGM-Ce structures was conducted using GESAMT[48] via the CCP4[49] interface over the phosphatase region (A/27–95 and A/339–538). Polder omit maps[50] were calculated with Phenix. Relevant crystallographic data are provided in Supplementary Table 1. Structures were further analyzed for binding interactions using Maestro (Schrödinger, LLC) by adding hydrogen atoms, followed by a rigid energy minimization using the OPLS4 force field[51].

Supplementary Material

Refer to Web version on PubMed Central for supplementary material.

Acknowledgements

We thank NCATS Research Services Core for archiving of peptides. We thank L. Lamy for expression plasmid preparation and E. Oliphant for data processing.

Funding.

This work was supported by the Japan Agency for Medical Research and Development (AMED), Platform Project for Supporting Drug Discovery and Life Science Research (Basis for Supporting Innovative Drug Discovery and Life Science Research) under JP21am0101090, and the Japan Society for the Promotion of Science (JSPS) Grant-in-Aid for Specially Promoted Research under JP20H05618 (H.S.). R.H.P.v.N. was supported by the Mitsubishi Corporation International Scholarship (JEES Sponsor-Crowned Scholarship) under scholarship number MITSU2011. This research was also supported in part by the Intramural Research Program of the National Center for Advancing Translational Sciences (NCATS), National Institutes of Health (NIH) under project 1ZIATR000247

(J.I.). This research used the IMCA-CAT beamline 17-ID at the Advanced Photon Source supported by the companies of the Industrial Macromolecular Crystallography Association through a contract with Hauptman-Woodward Medical Research Institute, the Advanced Photon Source supported by the U.S. Department of Energy (DOE), Office of Science, Office of Basic Energy Sciences, under Contract No. DE-AC02–06CH11357, and the NYX beamline (19-ID) of the National Synchrotron Light Source II, a U.S. Department of Energy (DOE) Office of Science User Facility operated for the DOE Office of Science by Brookhaven National Laboratory under Contract No. DE-SC0012704.

References

1. Bockus AT; Schwochert JA; Pye CR; Townsend CE; Sok V; Bednarek MA; Lokey RS, Going Out on a Limb: Delineating The Effects of beta-Branching, N-Methylation, and Side Chain Size on the Passive Permeability, Solubility, and Flexibility of Sanguinamide A Analogues. J Med Chem 2015, 58 (18), 7409–18. [PubMed: 26308180]
2. Chikhale EG; Ng KY; Burton PS; Borchardt RT, Hydrogen-Bonding Potential as a Determinant of the in-Vitro and in-Situ Blood-Brain-Barrier Permeability of Peptides. Pharmaceut Res 1994, 11 (3), 412–419.
3. Conradi RA; Hilgers AR; Ho NF; Burton PS, The influence of peptide structure on transport across Caco-2 cells. Pharm Res 1991, 8 (12), 1453–60. [PubMed: 1808606]
4. Furukawa A; Schwochert J; Pye CR; Asano D; Edmondson QD; Turmon AC; Klein VG; Ono S; Okada O; Lokey RS, Drug-Like Properties in Macrocycles above MW 1000: Backbone Rigidity versus Side-Chain Lipophilicity. Angew Chem Int Ed Engl 2020, 59 (48), 21571–21577. [PubMed: 32789999]
5. Haviv F; Fitzpatrick TD; Swenson RE; Nichols CJ; Mort NA; Bush EN; Diaz G; Bammert G; Nguyen A; Rhutasel NS, et al. , Effect of N-methyl substitution of the peptide bonds in luteinizing hormone-releasing hormone agonists. J Med Chem 1993, 36 (3), 363–9. [PubMed: 8381183]
6. Shinbara K; Liu W; van Neer RHP; Katoh T; Suga H, Methodologies for Backbone Macrocyclic Peptide Synthesis Compatible With Screening Technologies. Front Chem 2020, 8, 447. [PubMed: 32626683]
7. Kawakami T; Murakami H; Suga H, Messenger RNA-programmed incorporation of multiple N-methyl-amino acids into linear and cyclic peptides. Chem Biol 2008, 15 (1), 32–42. [PubMed: 18215771]
8. Yamagishi Y; Shoji I; Miyagawa S; Kawakami T; Katoh T; Goto Y; Suga H, Natural product-like macrocyclic N-methyl-peptide inhibitors against a ubiquitin ligase uncovered from a ribosome-expressed de novo library. Chem Biol 2011, 18 (12), 1562–70. [PubMed: 22195558]
9. Adessi C; Frossard MJ; Boissard C; Fraga S; Bieler S; Ruckle T; Vilbois F; Robinson SM; Mutter M; Banks WA, et al. , Pharmacological profiles of peptide drug candidates for the treatment of Alzheimer's disease. J Biol Chem 2003, 278 (16), 13905–11. [PubMed: 12578830]
10. Biron E; Chatterjee J; Ovadia O; Langenegger D; Brueggen J; Hoyer D; Schmid HA; Jelinek R; Gilon C; Hoffman A, et al. , Improving oral bioavailability of peptides by multiple N-methylation: somatostatin analogues. Angew Chem Int Ed Engl 2008, 47 (14), 2595–9. [PubMed: 18297660]
11. Werner HM; Cabalteja CC; Horne WS, Peptide Backbone Composition and Protease Susceptibility: Impact of Modification Type, Position, and Tandem Substitution. Chembiochem 2016, 17 (8), 712–8. [PubMed: 26205791]
12. Stanzel M; Schon A; Sprinzl M, Discrimination against misacylated tRNA by chloroplast elongation factor Tu. Eur J Biochem 1994, 219 (1–2), 435–9. [PubMed: 8307009]
13. Nissen P; Kjeldgaard M; Thirup S; Polekhina G; Reshetnikova L; Clark BF; Nyborg J, Crystal structure of the ternary complex of Phe-tRNAPhe, EF-Tu, and a GTP analog. Science 1995, 270 (5241), 1464–72. [PubMed: 7491491]
14. LaRiviere FJ; Wolfson AD; Uhlenbeck OC, Uniform binding of aminoacyl-tRNAs to elongation factor Tu by thermodynamic compensation. Science 2001, 294 (5540), 165–8. [PubMed: 11588263]
15. Iwane Y; Kimura H; Katoh T; Suga H, Uniform affinity-tuning of N-methyl-aminoacyl-tRNAs to EF-Tu enhances their multiple incorporation. Nucleic Acids Res 2021, 49 (19), 10807–10817. [PubMed: 33997906]

16. Huang Y; Wiedmann MM; Suga H, RNA Display Methods for the Discovery of Bioactive Macrocycles. Chem Rev 2019, 119 (17), 10360–10391. [PubMed: 30395448]
17. Passioura T; Suga H, A RaPID way to discover nonstandard macrocyclic peptide modulators of drug targets. Chem Commun (Camb) 2017, 53 (12), 1931–1940. [PubMed: 28091672]
18. Fothergill-Gilmore LA; Watson HC, The phosphoglycerate mutases. Adv Enzymol Relat Areas Mol Biol 1989, 62, 227–313. [PubMed: 2543188]
19. Roychowdhury A; Kundu A; Bose M; Gujar A; Mukherjee S; Das AK, Complete catalytic cycle of cofactor-independent phosphoglycerate mutase involves a spring-loaded mechanism. The FEBS journal 2015, 282 (6), 1097–110. [PubMed: 25611430]
20. Jedrzejas MJ, Structure, function, and evolution of phosphoglycerate mutases: comparison with fructose-2,6-bisphosphatase, acid phosphatase, and alkaline phosphatase. Progress in biophysics and molecular biology 2000, 73 (2–4), 263–87. [PubMed: 10958932]
21. Crowther GJ; Booker ML; He M; Li T; Raverdy S; Novelli JF; He P; Dale NR; Fife AM; Barker RH Jr., et al. , Cofactor-independent phosphoglycerate mutase from nematodes has limited druggability, as revealed by two high-throughput screens. PLoS neglected tropical diseases 2014, 8 (1), e2628. [PubMed: 24416464]
22. Wiedmann M; Dranchak PK; Aitha M; Queme B; Collmus CD; Kashipathy MM; Kanter L; Lamy L; Rogers JM; Tao D, et al. , Structure-activity relationship of ipglycermide binding to phosphoglycerate mutases. J Biol Chem 2021, 296, 100628. [PubMed: 33812994]
23. Yu H; Dranchak P; Li Z; MacArthur R; Munson MS; Mehzabeen N; Baird NJ; Battalie KP; Ross D; Lovell S, et al. , Macrocycle peptides delineate locked-open inhibition mechanism for microorganism phosphoglycerate mutases. Nat Commun 2017, 8, 14932. [PubMed: 28368002]
24. Nowicki MW; Kuaprasert B; McNae IW; Morgan HP; Harding MM; Michels PA; Fothergill-Gilmore LA; Walkinshaw MD, Crystal structures of Leishmania mexicana phosphoglycerate mutase suggest a one-metal mechanism and a new enzyme subclass. Journal of molecular biology 2009, 394 (3), 535–43. [PubMed: 19781556]
25. Dutow P; Schmidl SR; Ridderbusch M; Stülke J, Interactions between Glycolytic Enzymes of Mycoplasma pneumoniae. Journal of Molecular Microbiology and Biotechnology 2010, 19 (3), 134–139. [PubMed: 20924199]
26. Foster JM; Davis PJ; Raverdy S; Sibley MH; Raleigh EA; Kumar S; Carlow CK, Evolution of bacterial phosphoglycerate mutases: non-homologous isofunctional enzymes undergoing gene losses, gains and lateral transfers. PLoS One 2010, 5 (10), e13576. [PubMed: 21187861]
27. Murakami H; Ohta A; Ashigai H; Suga H, A highly flexible tRNA acylation method for non-natural polypeptide synthesis. Nat Methods 2006, 3 (5), 357–9. [PubMed: 16628205]
28. Goto Y; Ohta A; Sako Y; Yamagishi Y; Murakami H; Suga H, Reprogramming the translation initiation for the synthesis of physiologically stable cyclic peptides. ACS Chem Biol 2008, 3 (2), 120–9. [PubMed: 18215017]
29. Goto Y; Katoh T; Suga H, Flexizymes for genetic code reprogramming. Nat Protoc 2011, 6 (6), 779–90. [PubMed: 21637198]
30. Shimizu Y; Inoue A; Tomari Y; Suzuki T; Yokogawa T; Nishikawa K; Ueda T, Cell-free translation reconstituted with purified components. Nat Biotechnol 2001, 19 (8), 751–5. [PubMed: 11479568]
31. Passioura T; Katoh T; Goto Y; Suga H, Selection-based discovery of druglike macrocyclic peptides. Annu Rev Biochem 2014, 83, 727–52. [PubMed: 24580641]
32. Collins JM; Porter KA; Singh SK; Vanier GS, High-efficiency solid phase peptide synthesis (HE-SPPS). Org Lett 2014, 16 (3), 940–3. [PubMed: 24456219]
33. Biron E; Chatterjee J; Kessler H, Optimized selective N-methylation of peptides on solid support. J Pept Sci 2006, 12 (3), 213–9. [PubMed: 16189816]
34. Katoh T; Sengoku T; Hirata K; Ogata K; Suga H, Ribosomal synthesis and de novo discovery of bioactive foldamer peptides containing cyclic beta-amino acids. Nat Chem 2020, 12 (11), 1081–1088. [PubMed: 32839601]
35. Fairhead M; Howarth M, Site-specific biotinylation of purified proteins using BirA. Methods Mol Biol 2015, 1266, 171–84. [PubMed: 25560075]
36. Huynh K; Partch CL, Analysis of protein stability and ligand interactions by thermal shift assay. Curr Protoc Protein Sci 2015, 79, 28 9 1–28 9 14.

37. Gorrec F, The MORPHEUS protein crystallization screen. J Appl Crystallogr 2009, 42 (Pt 6), 1035–1042. [PubMed: 22477774]
38. Kabsch W, Automatic-Indexing of Rotation Diffraction Patterns. J Appl Crystallogr 1988, 21, 67–71.
39. Kabsch W, Xds. Acta Crystallogr D 2010, 66, 125–132. [PubMed: 20124692]
40. Vonrhein C; Flensburg C; Keller P; Sharff A; Smart O; Paciorek W; Womack T; Bricogne G, Data processing and analysis with the autoPROC toolbox. Acta Crystallogr D 2011, 67, 293–302. [PubMed: 21460447]
41. Evans PR, An introduction to data reduction: space-group determination, scaling and intensity statistics. Acta Crystallogr D 2011, 67, 282–292. [PubMed: 21460446]
42. McCoy AJ; Grosse-Kunstleve RW; Adams PD; Winn MD; Storoni LC; Read RJ, Phaser crystallographic software. J Appl Crystallogr 2007, 40, 658–674. [PubMed: 19461840]
43. Cowtan K, The Buccaneer software for automated model building. 1. Tracing protein chains. Acta Crystallogr D Biol Crystallogr 2006, 62 (Pt 9), 1002–11. [PubMed: 16929101]
44. Adams PD; Afonine PV; Bunkoczi G; Chen VB; Davis IW; Echols N; Headd JJ; Hung LW; Kapral GJ; Grosse-Kunstleve RW, et al. , PHENIX: a comprehensive Python-based system for macromolecular structure solution. Acta Crystallogr D 2010, 66, 213–221. [PubMed: 20124702]
45. Emsley P; Lohkamp B; Scott WG; Cowtan K, Features and development of Coot. Acta Crystallogr D 2010, 66, 486–501. [PubMed: 20383002]
46. Chen VB; Arendall WB; Headd JJ; Keedy DA; Immormino RM; Kapral GJ; Murray LW; Richardson JS; Richardson DC, MolProbity: all-atom structure validation for macromolecular crystallography. Acta Crystallogr D 2010, 66, 12–21. [PubMed: 20057044]
47. Potterton L; McNicholas S; Krissinel E; Gruber J; Cowtan K; Emsley P; Murshudov GN; Cohen S; Perrakis A; Noble M, Developments in the CCP4 molecular-graphics project. Acta Crystallogr D 2004, 60, 2288–2294. [PubMed: 15572783]
48. Krissinel E, Enhanced fold recognition using efficient short fragment clustering. Journal of Molecular Biochemistry 2012, 1 (2), 76–85. [PubMed: 27882309]
49. Winn MD; Ballard CC; Cowtan KD; Dodson EJ; Emsley P; Evans PR; Keegan RM; Krissinel EB; Leslie AGW; McCoy A, et al. , Overview of the CCP4 suite and current developments. Acta Crystallogr D 2011, 67, 235–242. [PubMed: 21460441]
50. Liebschner D; Afonine PV; Moriarty NW; Poon BK; Sobolev OV; Terwilliger TC; Adams PD, Polder maps: improving OMIT maps by excluding bulk solvent. Acta Crystallogr D Struct Biol 2017, 73 (Pt 2), 148–157. [PubMed: 28177311]
51. Lu C; Wu C; Ghoreishi D; Chen W; Wang L; Damm W; Ross GA; Dahlgren MK; Russell E; Von Bargen CD, et al. , OPLS4: Improving Force Field Accuracy on Challenging Regimes of Chemical Space. J Chem Theory Comput 2021, 17 (7), 4291–4300. [PubMed: 34096718]

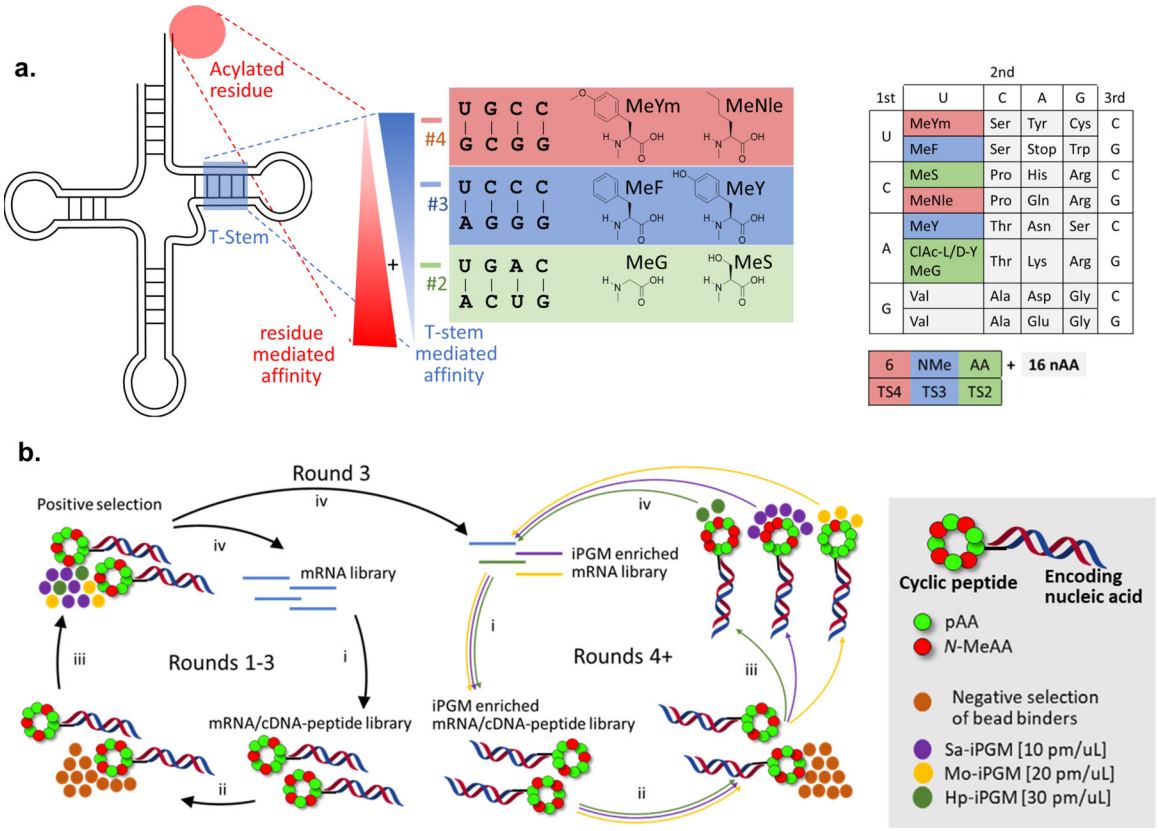

Figure 1. tRNA tuning approach of *N*-MeAA incorporation using "pool-and-split" RaPID selection paradigm.

(**a**) *N*-methyl amide amino acid codons. (**b**) RaPID selection where rounds 1–3 utilize the pooled procaryotic iPGMs, whereas rounds 4 onward continue the selection process using individual iPGMs and the enriched library. (i) Puromycin ligation, *in vitro* translation, and reverse transcription. (ii) Negative selection of bead binders. (iii) Affinity selection with pooled or individual iPGMs. (iv) Transcription of enriched DNA sequences.

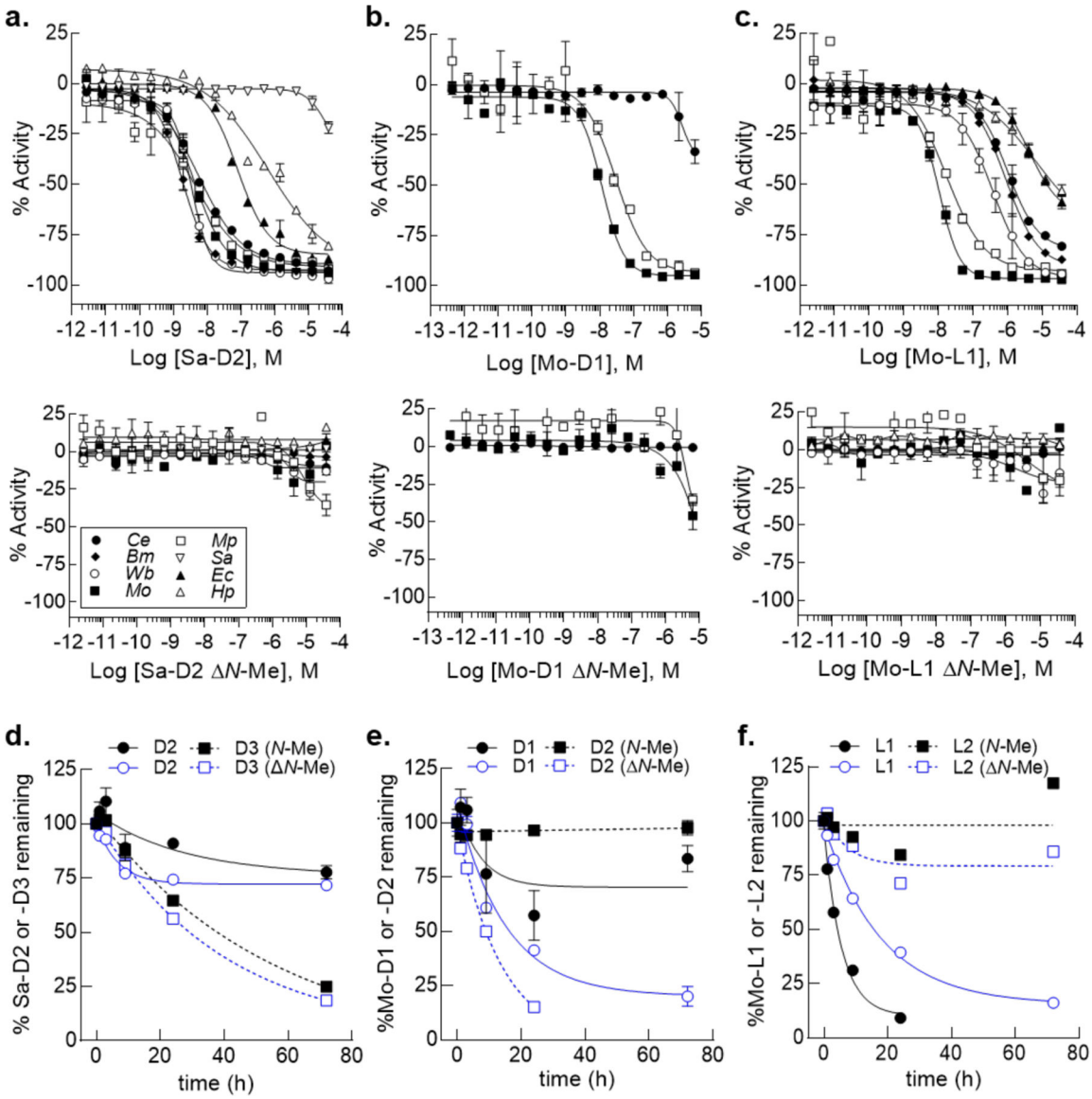

Figure 2. Comparative functional and human serum stability characterization of select Sa-D and Mo-L/D synthetic cyclic peptides and Δ*N*-Me analogs.

(**a–c**) MCP CRCs on representative iPGM orthologs from bacteria, *S. aureus* (*Sa*), *E. coli* (*Ec*), *H. pylori* (*Hp*), *M. orale* (*Mo*) and *M. pneumonia* (*Mp*) and nematode, *C. elegans* (*Ce*), *B. malayi* (*Bm*) and *W. bancrofti* (*Wb*). Top plots represent *N*-Me containing MCPs and bottom plots correspond to Δ*N*-Me analogs. Data are representative of N≥3 independent experiments. (**d–f**). MCP stability time course where solid symbols represent *N*-methyl amide-containing MCPs and open symbols the corresponding amide analogs, where solid dashed lines represent analog pairs. MCPs pairs containing an internal standard peptide were incubated with human serum at 37°C as described in materials and methods. At 0, 1, 3, 9, 24, and 72 h, the human serum was reduced with 10 mM TCEP and relative intensity of each peptide to the standard peptide was determined by LC/MS. Relative intensity at 0 h was defined as 100%. The experimental data were fitted by non-linear regression one phase decay curve using GraphPad Prism 9.2.0.

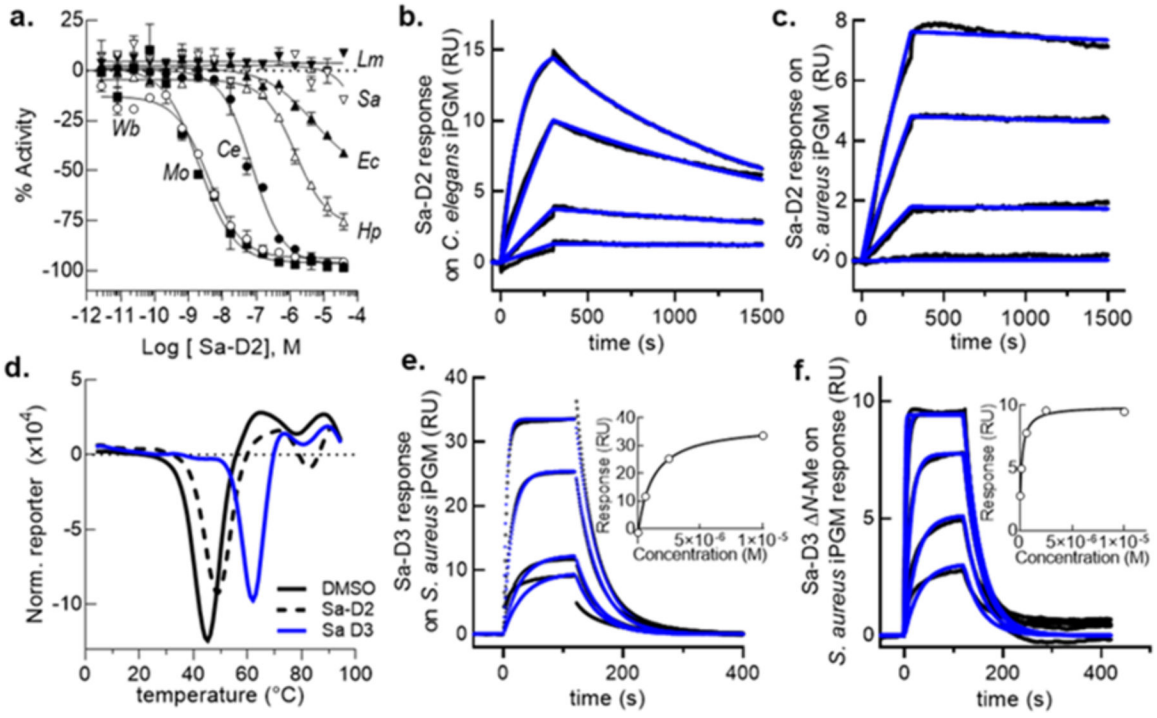

Figure 3. Functional, binding kinetics and thermal stability characterization of Sa-D2 and –D3 cyclic peptides and analogs.

(**a**) CRCs for activity of Sa-D2 on representative iPGM orthologs from the protozoan *L. mexicana* (*Lm*); bacteria *S. aureus* (*Sa*), *E. coli* (*Ec*), *H. pylori* (*Hp*) and *M. orale* (*Mo*), and nematode *C. elegans* (*Ce*) and *W. bancrofti* (*Wb*). (**b**, **c**) Sensorgrams for Sa-D2 (0.5 – 31 nM) or Sa-D2 (8 – 500 nM) binding kinetics derived from a *C. elegans* or *S. aureus* iPGM, respectively, conjugated sensor chip surface. (**d**) First derivative plots of the fluorescence emission as a function of temperature for either Sa-D2 (dashed line, T_m=48.7°C) or Sa-D3 (blue line, T_m=62.4°C) binding to *S. aureus* iPGM vs DMSO control (black line, T_m=45.7°C). (**e**, **f**) Sensorgrams for Sa-D3 (156 nM - 10 μM; K_D=790 nM, $t_{½}$ =27s) and Sa-D3 Δ*N*-Me (39 nM - 10 μM; K_D=280 nM, $t_{½}$ =25s) binding kinetics and saturation binding curve (inset) for *S. aureus* iPGM. The experimental SPR data (black) were globally fit to a 1:1 binding model (blue lines) using BIAevaluation, as described in Experimental procedures, to determine kinetic rate constants. Corresponding insets show the signal observed at equilibrium, R_{eq}, plotted as a function of the [MCP], fit to a hyperbolic, single-site binding equation. Data are representative of N≥3 independent experiments.

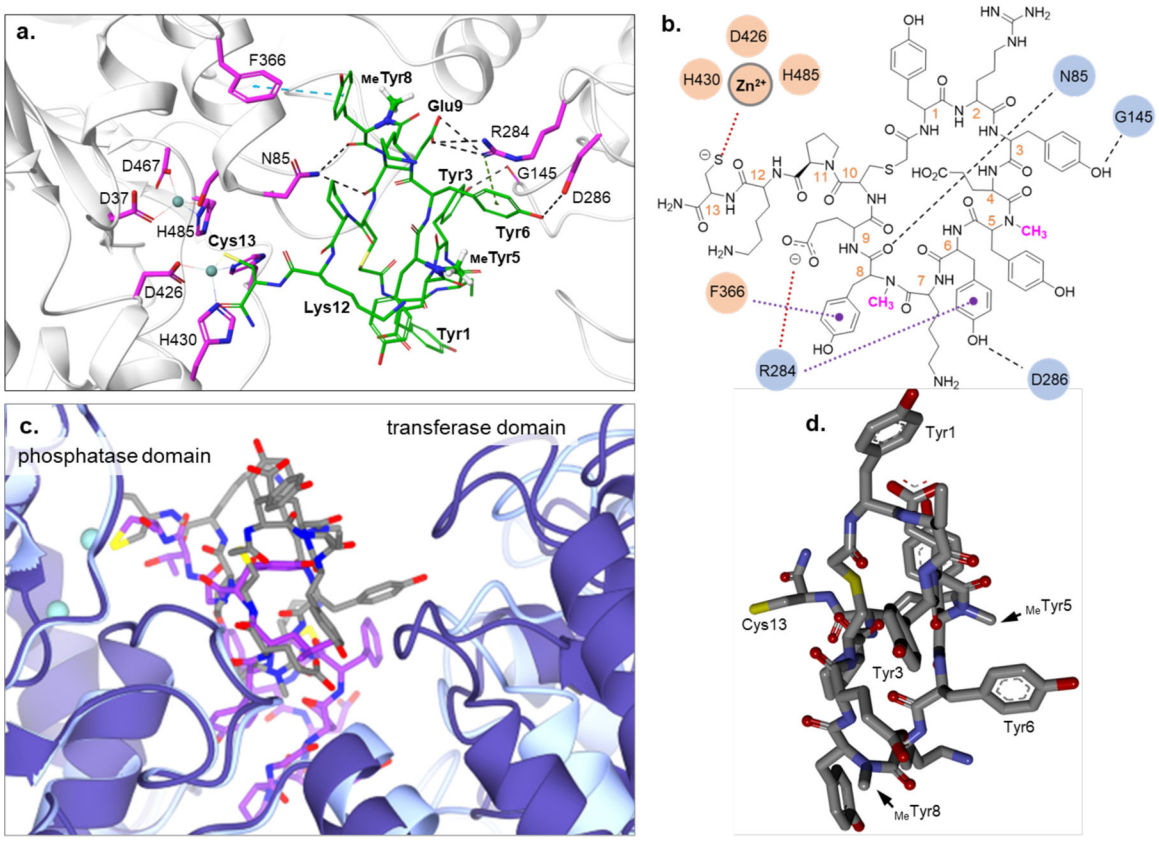

Figure 4. Ipglycermides Ce-2 Y7F and Sa-D2 have unique *C. elegans* iPGM Zn^{2+}-coordinating binding modes.

(**a**) Key protein-ligand interactions and Cys13 – Zn^{2+} coordination observed between Sa-D2 and *C. elegans* iPGM. *N*-Me amides are shown with hydrogens (white) for clarity. (**b**) Two-dimensional protein-cyclic peptide pharmacophore interactions. Phosphatase (apricot) and phosphotransferase (pastel blue) domain are indicated having H-bonding (black dashes), ionic (red dots), or π-cation (purple dots) interactions. (**c**) Superposition of *C. elegans* iPGM•Sa-D2 (dark blue/dim grey; PDB: 7TL7) and *C. elegans* iPGM•Ce-2 Y7F (ice blue/violet; PDB: 7KNG) structures fixed over the amino acid range of 27–95 and 339–538 (phosphatase domain). Zn^{2+} ions are sea blue. (**d**) Conformation of Sa-D2 as bound to *C. elegans* iPGM, with the two *cis N*-methyl amides at Tyr6 and Tyr8 indicated by arrows.

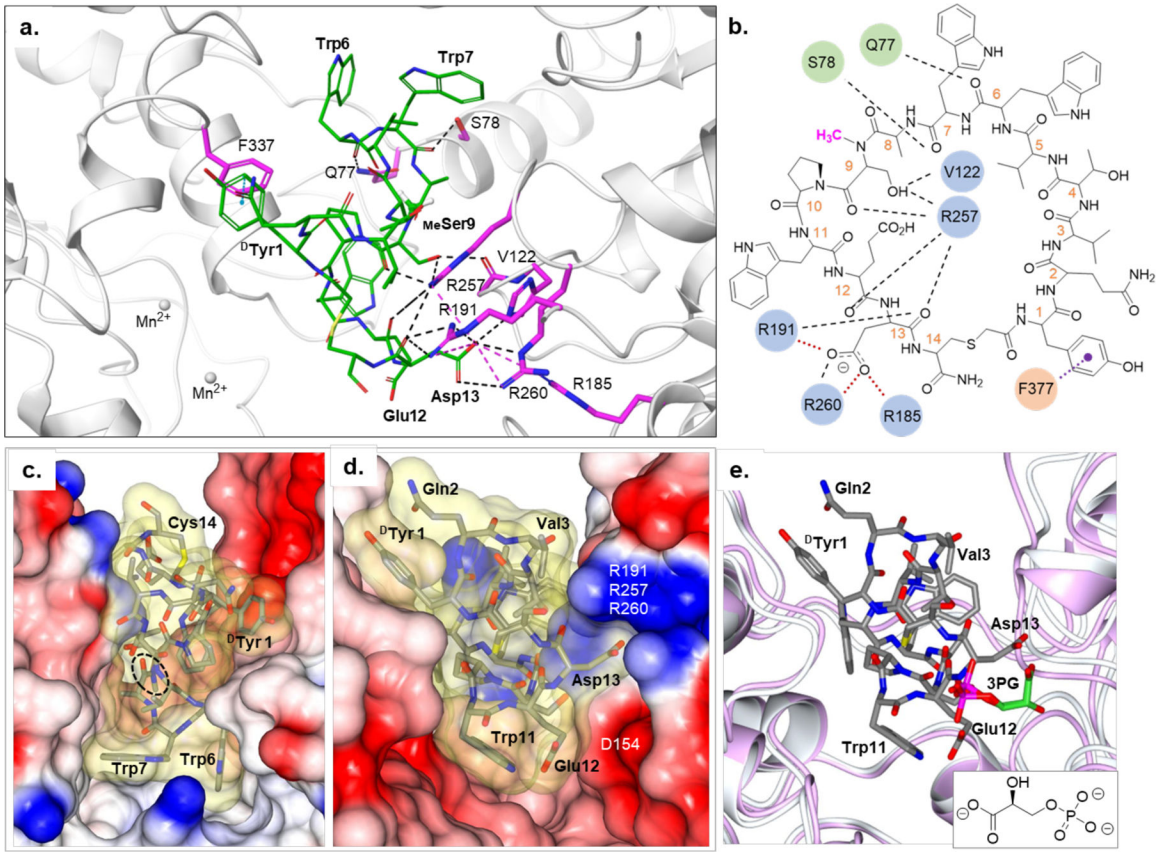

Figure 5. Sa-D3 ipglycermide partially mimic 3PG binding to *S. aureus* iPGM.

(**a**) Conformation of Sa-D3 as bound to *S. aureus* iPGM, showing the *trans N*-methyl amide at $_{Me}$Ser9 (shown with *N*-Me hydrogens (white) for clarity) and Asp13 interaction with R185, R191, R257 and R260 of the 3-phosphoglycerate (3PG) binding site. (**b**) Two-dimensional protein-cyclic peptide pharmacophore interactions. Phosphotransferase (pastel blue) domain and Hinge regions (celadon) are indicated having H-bonding (black dashes) or ionic (red dots) interactions. An edge-face aromatic F377 interaction from the phosphatase domain (apricot) is shown by purple dots. (**c**) Electrostatic surface representation of *S. aureus* iPGM • Sa-D3 complex where the cyclic peptide (grey) surface is rendered in yellow and the *trans N*-methyl amide circled. (**d**) Same as panel c but rotated 90° about horizontal axis to show 3PG binding site. (**e**) Superposition of the *S. aureus* iPGM - Sa-D3 (white; PDB: 7TL8) with 3PG bound (PDB 4NWJ) *S. aureus* iPGM (lilac). The Sa-D3 cyclic peptide is rendered as grey, and 3PG as green/magenta cylinders (chemical structure shown in inset). Prepared with CCP4MG, version 2.10.10.

ACS Chem Biol. Author manuscript; available in PMC 2023 August 19.

Table 1.

Sequence and activity of prokaryotic iPGM-derived *N*-methyl amide macrocyclic

MCP ID	MCP Sequence	pAC$_{50\ apparent\ \pm sd}$															
		Nematode				Bacterium											
		C. elegans		*B. malayi*		*W. bancrofti*		*M. orale*		*M. pneumoniae*		*E. coli*		*s. aureus*		*H. pylori*	
Ce-2	^{Ac}yDYPGDYCYLYGTC	**8.61**	0.03	**8.57**	0.06	**8.63**	0 09	na	-	na	-	6.50	0.10	na	-	5.44	002
Ce-2$_{act}$																6 78	0 15
Ce-2d	^{Ac}yDYPGDYCYLY	**8.54**	0.05	7.35	0 08	7.33	0 12	na	-	na	-	na	-	na	-	na	-
Hp-L2	^{Ac}Y$_{Me}$Y$^{(OMe)}$R$_{Me}$FD$_{Me}$S$_{Me}$YQS$_{Me}$S$_{Me}$Y$^{(OMe)}$V$_{Me}$Y$_{Me}$NlePC	5.19	0.13	5.21	0.25	5.25	0.53	5.73	005	5.84	nd	5.51	0.03	na	-	5 22	0 10
Hp-D3	^{Ac}yDSYA$_{Me}$Y$^{(OMe)}$$_{Me}Y_{Me}FNG_{Me}$YNHYWC	7.81	0.07	7.61	0.06	7.09	0.03	5.69	008	5.92	0.03	6.93	0.10	na	-	6.01	006
Hp-D3 ΔMe	^{Ac}yDSYA_Y$^{(OMe)}$_Y_FNG_YNHYWC	na	-	na	-	na	-	na	-	<5	-	na		na	-	na	-
Hp-D4	^{Ac}yYWQ$_{Me}$Y$_{Me}$YEYGY$_{Me}$YKC	4.87	0.04	5.44	0.06	6.33	0.06	5.92	004	4.85	020	5.20	0.18	na	-	5.84	0.10
Mo-L1	^{Ac}Y$_{Me}$Y$_{Me}$FYD$_{Me}$F$_{Me}$YGN$_{Me}$YSYRVPC	6.03	0.03	6.09	0.03	6.51	0.06	**8.03**	0.18	7.80	007	5.36	0.10	na	-	5.23	0.17
Mo-L1 ΔMe	^{Ac}Y_Y_FYD_F_YGN_YSYRVPC	na	-	na	-	4.78	nd	4.75	0.14	4.75	nd	na	-	na	-	na	-
Mo-L2	^{Ac}YPDTNWWY$_{Me}$YDEWHC	na	-	na		5.84	026	**8.61**	0.20	**8.73**	0.14	na	-	na	-	na	-
Mo-L2 ΔMe	^{Ac}YPDTNWWY_YDEWHC	na	-	na	-	4.48	nd	5.48	0.27	5.42	0.15	na		na	-	na	-
Mo-D1	^{Ac}ySGDWWY$_{Me}$YDEW$_{Me}$SVA$_{Me}$F$_{Me}$GC	na	-	4.88	nd	na	-	**8.21**	028	7.61	007	na	-	na	-	na	-
Mo-D1 ΔMe	^{Ac}ySGDWWY_YDEW_SVA_F_GC	na	-	na	-	4.25	nd	4.93	0.12	4.59	021	na	-	na	-	na	-
Mo-D2	^{Ac}yW$_{Me}$YD$_{Me}$S$_{Me}$Y$_{Me}$Y$^{(OMe)}$YPGTAQ$_{Me}$YTC	4.46	0.56	4.46	0.15	na	-	7.99	0.20	7.17	0.09	na	-	na	-	na	-
Mo-D2 ΔMe	^{Ac}yW_YD_S_Y_Y$^{(OMe)}$YPGTAQ_YTC	na	-	na	-	4.57	nd	4.72	0.04	4.65	0.05	na	-	na	-	na	-
Sa-L2	^{Ac}Y$_{Me}$Y$^{(OMe)}$NDSGW$_{Me}$YNT$_{Me}$FC	5.56	004	4.08	0.01	4.34	nd	4.34	003	4.37	0.08	5.16	0.12	6.76	0.06	na	-
Sa-D2	^{Ac}yRYE$_{Me}$YYK$_{Me}$YECPKCC	**8.35**	0.10	**8.74**	0.05	**8.57**	0.13	**8.55**	0.19	**8.65**	0.30	7.21	0.10	na	-	6.40	021
Sa-D2 ΔMe	^{Ac}yRYE_YYK_YECPKC	na	-	na	-	4.69	nd	4.61	0.12	4.71	0.08	na	-	na	-	na	-
Sa-D2 C13S	^{Ac}yRYE$_{Me}$YYK$_{Me}$YECPKS	4.96	0.09	4.83	0.03	5.45	0.11	5.26	0.56	5.08	0.06	na	-	na	-	na	-

MCP ID	MCP Sequence	$pAC_{50\ apparent\ \pm sd}$															
		Nematode				Bacterium											
		C. elegans		*B. malayi*		*W. bancrofti*		*M. orale*		*M. pneumoniae*		*E. coli*		*s. aureus*		*H. pylori*	
Sa-D2 ΔPKC	^{Ac}yRYE$_{Me}$YYK$_{Me}$YEC	na	-	na	-	5.26	0.61	<5	nd	5.29	0.44	na		na	-	na	-
Sa-D2 LgMC	^{Ac}yRYE$_{Me}$YYK$_{Me}$YECPKC	5.40	0.08	5.77	0.14	5.77	0.13	5.97	0.08	5.85	0.21	4.73	0.07	na	-	4.48	0.08
Sa-D2 LgMC ΔMe	^{Ac}yRYE_YYK_YECPKC	na	-	na	-	na	-	na	-	na	-	na	-	na	-	na	-
Sa-D3	^{Ac}yQVTVWWA$_{Me}$SPWEDC	na	-	na		4.92	0.57	**8.58**	0.17	**8.32**	0.15	na		7.42	0.09	na	-
Sa-D3 ΔMe	^{Ac}yQVTVWWA_SPWEDC	na	-	na	-	na	-	**8.10**	0.15	6.79	042	na	-	7.40	0.04	na	-

Notes: pAC_{50} in bold indicated potent nM activity and pAC_{50} in italics indicates the activation of *H.p.* iPGM by Ce-2 from a biphasic response. Macrocycle is formed between Ac and cystine in blue, N-methyl amino acids are indicated in red. All MCPs were inactive on the protozoan, *L. Mexicana*. 'na' indicates no measurable inhibitory activity. The error, reported as s.d., represent determinations from N≥3 experiments. Error was not determined, nd, when partial curves fits were only obtained from one of the experimental replicates due to a low MCP inhibitory activity.